J. Fluid Mech. (2025), *vol.* 1019, A24, doi:10.1017/jfm.2025.10585

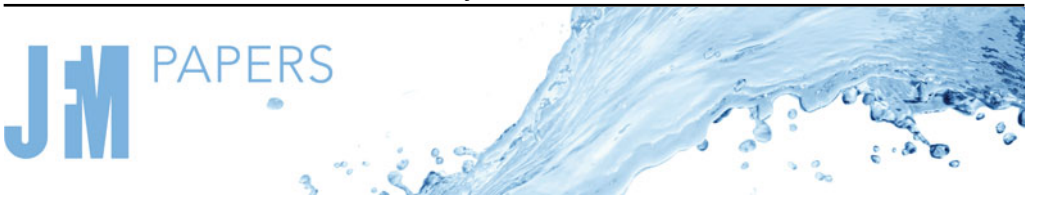

Universal thermodynamic bounds and entropy production of interscale amplitude modulation in turbulent boundary layers

Giovanni Iacobello

School of Engineering, University of Surrey, Guildford GU2 7XH, UK

Corresponding author: Giovanni Iacobello, g.iacobello@surrey.ac.uk

(Received 21 January 2025; revised 11 August 2025; accepted 12 August 2025)

A discrete Markov model is proposed to study the interscale dynamics of high Reynolds number wall turbulence. The amplitude modulation of the small turbulent scales due to the interaction with large turbulent scales is investigated for three experimental turbulent boundary layers. Through an appropriate discretisation of the turbulence signals, recently proved universal thermodynamic bounds for discrete-state stochastic systems are shown to apply to continuous-state systems like turbulence, regardless of the distance from the wall and the Reynolds number. Adopting Schnakenberg's network theory for stochastic processes, we provide evidence for a direct proportionality relation between the mean cycle affinity-based entropy production rate (a stochastic thermodynamic quantity) and a mean entropy production rate associated with the net large-to-small-scale turbulent kinetic energy production. Finally, new insights into the relative arrangement (lag/lead) between large and small scales are provided.

Key words: turbulent boundary layers, turbulence modelling, turbulence theory

1. Introduction

Fluid flows have been the subject of several works adopting theories and tools from stochastic thermodynamics (Seifert 2012; Falasco & Esposito 2025). Most notably, the celebrated fluctuation theorem was initially tested on shear flows (Evans, Cohen & Morriss 1993). The significant link between fluid flows and stochastic thermodynamics becomes even more apparent when turbulent flows are investigated, as turbulence naturally suits the (stochastic) thermodynamic formalism owing to its random-like nature and non-equilibrium properties (Peinke, Tabar & Wächter 2019). Outstanding results in this context

include, among others, the verification of various forms of the fluctuation theorem in turbulent flows (Ciliberto *et al.* 2004; Nickelsen & Engel 2013; Fuchs *et al.* 2020; Porporato *et al.* 2020; Yao *et al.* 2023, 2024), the emergence of Markovian features of the turbulence energy cascade (Friedrich & Peinke 1997; Peinke *et al.* 2019) and its implication for small-scale turbulence (Renner *et al.* 2002, 2006; Reinke *et al.* 2018), as well as the broken asymmetry (irreversibility) in the statistics of turbulence quantities from a Lagrangian (Jucha *et al.* 2014; Xu *et al.* 2014; Polanco *et al.* 2018) and an Eulerian (Zorzetto, Bragg & Katul 2018; Drivas 2019; Cheminet *et al.* 2022; Iacobello *et al.* 2023; Schmitt 2023) viewpoint.

Although the interdisciplinary connection between turbulence and stochastic thermodynamics has been an active area of research (Peinke *et al.* 2019), several open issues remain, e.g. under which circumstances the stochastic thermodynamics formalisms can be applied to investigate the complex turbulence interscale energetic processes. The problem is further complicated when wall-bounded turbulent flows are considered, owing to the explicit dependence of the flow properties on one or more spatial coordinates. In wall-bounded turbulence, in fact, energetic processes take place both in the scale space (at fixed spatial location) and the physical, three-dimensional, space where organised fluid motion develops over time (Jiménez 2018). This study aims to adopt a stochastic thermodynamics framework to shed more light on the energetic processes at play in turbulent boundary layers. A discrete Markov model and Schnakenberg's network theory for stochastic processes in non-equilibrium steady state (Schnakenberg 1976; Andrieux & Gaspard 2007) are adopted here, to investigate the amplitude modulation (AM) interscale interaction in turbulent boundary layers at a high Reynolds number. The AM in turbulence consists of an interscale interaction mechanism, where the amplitude of the smaller turbulent scales tends to be enhanced or dampened by the behaviour of the larger turbulent scales (Hutchins & Marusic 2007; Marusic, Mathis & Hutchins 2010; Andreolli *et al.* 2023).

Interscale AM in turbulent flows has been studied in the last two decades (Hutchins & Marusic 2007; Mathis *et al.* 2009*a*), but the mechanisms behind this phenomenon are far from being fully understood (see, among others, Mathis *et al.* 2009*b*; Ganapathisubramani *et al.* 2012; Agostini & Leschziner 2014; Talluru *et al.* 2014; Baars *et al.* 2015; Duvvuri & McKeon 2015; Anderson 2016; Squire *et al.* 2016). For instance, the energetic processes at play that generate and sustain such a modulation phenomenon, and what tools of analysis can effectively capture key features of AM, are still subjects of research (Dogan *et al.* 2019; Andreolli *et al.* 2023). Nevertheless, advancing our understanding of AM – alongside frequency modulation (Baars *et al.* 2015; Iacobello, Ridolfi & Scarsoglio 2021) – in turbulent flows has significant implications, not only from a theoretical perspective but also for deploying more effective control strategies for drag reduction that have a major impact on several transportation and energy systems such as aircraft, ships and wind farms (Marusic *et al.* 2021).

Specifically, here we address the following two questions.

(i) Which turbulence quantity – equivalent to a thermodynamic force – drives the interscale AM process out of equilibrium?
(ii) Do universal thermodynamic bounds hold for high Reynolds number turbulence processes like AM?

We show here that the net large-to-small-scale turbulent kinetic energy production is the main turbulent quantity that can be associated with an analogous thermodynamic force driving the AM process out-of-equilibrium (question (i)). In particular, the entropy generation rate associated with the AM is provided in both the stochastic thermodynamics

and fluid dynamics formalism, and the two formulations are shown to be equivalent to a proportionality factor. Moreover, we show that universal thermodynamic bounds hold for high Reynolds number turbulent boundary layers (question (ii)). Such bounds refer to the asymmetry of the two-time cross-correlations between two variables at a given temporal lag, where such an asymmetry is a fundamental statistical signature of systems in non-equilibrium steady state (Ohga, Ito & Kolchinsky 2023). Although question (ii) may appear to be disconnected from question (i), the bounding quantity – that is, the cycle affinity – is strictly related to the entropy generation rate, and the verification of the aforementioned bounds provides supporting evidence for the applicability of the proposed model.

It is worth highlighting that, the verification of thermodynamic bounds (question (ii)) for high Reynolds number turbulence represents a notable outcome that can have significant implications for studying turbulent flows beyond AM, due to the ubiquitous adoption of temporal cross-correlation in turbulence analysis (Jachens *et al.* 2006; Wallace 2014).

To answer the questions (i) and (ii) above, three turbulent boundary layer datasets are exploited, which are detailed in § 2. The Markov model is described in § 3, and results are presented in § 4. In particular, the applicability of thermodynamic bounds in wall turbulence is discussed in § 4.1, the entropy production rate associated with the large-small scale AM is discussed in § 4.2, while insights into the large-small scale arrangement are discussed in § 4.3. Concluding remarks and future outlook are finally reviewed in § 5.

2. Amplitude modulation quantification and dataset details

Interscale AM is quantified, following previous studies (Mathis *et al.* 2009*a*), as the cross-correlation coefficient $C_{LS} = \mathrm{Corr}[u_L(t), E_{S,L}(t)]$ between the large-scale streamwise velocity signal, $u_L(t)$, and the low-pass filtered envelope fluctuations (zero mean), $E_{S,L}(t)$, of the small-scale streamwise velocity signal $u_S(t)$. Specifically, the signal $E_{S,L}(t)$ is calculated – following Mathis *et al.* (2009*a*) – by evaluating the envelope $E_S(t)$ of the small-scale signal u_S, and then applying a long-wavelength pass-filter to $E_S(t)$ with the same cutoff wavelength used to separate u_L and u_S (see more filtering details below).

Accordingly, u_L and $E_{S,L}$ are the two key variables used to represent the AM phenomenon. Although other approaches have been proposed to quantify AM (Dogan *et al.* 2019), the correlation-based method is able to capture the key features of AM in turbulence.

Three experimental datasets of turbulent boundary layers over a smooth wall are employed at frictional Reynolds number $Re_* = 2200$ (TBL2k), $Re_* = 13\,300$ (TBL13k) and $Re_* = 14\,750$ (TBL14k), where $Re_* = U_*\delta/\nu$, U_* is the frictional velocity, δ is the boundary layer thickness and ν is the kinematic viscosity. Experiments provide an easier way to reach higher Re_* compared with numerical simulations, where spatial snapshots are instead usually stored. For each experiment, time series of the streamwise velocity, $u'(y, t)$ are available at various wall-normal coordinates, y, and time t.

To decompose the streamwise velocity signals into their small- and large-scale components, u_S and u_L, a Fourier filtering approach is adopted such that $u(t) = u_L(t) + u_S(t)$ (Dogan *et al.* 2019), where $u(y, t) = u'(y, t) - U(y)$ and U is the mean velocity. Cutoff wavelengths in the range $\lambda_{x,co}/\delta = 1, \ldots, 5$ are used, and Taylor's hypothesis is adopted to get $\lambda_{x,co}$ from time series data, namely $\lambda_{x,co} = U(y)/f_{co}$, where f_{co} is the cutoff frequency. Although the applicability of Taylor's hypothesis in wall turbulence is still the subject of ongoing research (e.g. see Squire *et al.* 2017), the local mean velocity U has been extensively used as the convection velocity, U_{conv}, to convert time series into spatial series. An alternative choice for U_{conv} was provided by Yang & Howland (2018) in the context of modulation in wall turbulence, where they proposed to use $U_{conv} = u'(t, y)$

label	Re_*	T_{min}	N_{ea}	f_s^+	y_{min}^+	# sensors
TBL14k	14 750	94	12	0.783	10.45	One-point
TBL13k	13 300	122	10	1.63	10.53	Two-point
TBL2k	2200	88	10	3.44	9.72	One-point

Table 1. Main parameters for the three turbulent boundary layer datasets.

to quantify the AM, due to a dependence of the AM coefficient on the intensity of turbulence fluctuations. This choice of the convection velocity is tested in this work, and results for $U_{conv} = u'$ are reported and discussed in Appendix A.

It is worth noting that, $\lambda_{x,co}/\delta = 1$ is the minimum value that effectively separates small- and large-scale motions (Mathis *et al.* 2009*a*), while $\lambda_{x,co}/\delta = 5$ is taken as the upper threshold as previous works have reported $\lambda_{x,co}/\delta \approx 6$ as a typical (maximum) length of large-scale motion in turbulent boundary layers (Mathis *et al.* 2009*a*). Moreover, TBL2k represents a lower limit for Re_*, since $Re_* \gtrsim 2000$ has been indicated as a lower bound to effectively observe large-small scale separation (Hutchins & Marusic 2007).

Table 1 includes some details for the three datasets that are relevant to the present study. The quantity $T_{min} = TU_{min}/\lambda_{x,co;max}$ is the minimum number of times the cutoff wavelength $\lambda_{x,co}$ is contained in the signal length TU across the boundary layer height, where $U_{min} = U(y_{min})$ is the mean velocity at the minimum wall normal location y_{min}, and $\lambda_{x,co;max}$ is the maximum cutoff value. Table 1 indicates that the cutoff wavelength is contained at least 88 times for TBL2k, and even more for the other datasets, thus ensuring that the signal is long enough. Here N_{ea} (fourth column in table 1) is the number of different samples used for ensemble averaging the results as indicated by the $\langle\bullet\rangle$ notation. For the TBL14k case, since three sets of measurements are available, each time series is split into four non-overlapping signals leading to a total of $N_{ea} = 12$ signal segments at each y coordinate. For the TBL13k and TBL2k cases, instead, only one experimental run is available. Therefore, time series from the TBL13k and TBL2k datasets are split into $N_{ea} = 10$ non-overlapping signal segments at each y coordinate. A discussion on the effect of N_{ea} and T_{min} is reported in Appendix C.

The sampling frequency and the first wall-normal coordinate are, respectively, $f_s^+ = f_s\nu/U_*^2$ and $y_{min}^+ = y_{min}U_*/\nu$, where the $+$ superscript signifies normalisation in wall units. Finally, the last column in table 1 indicates the number of synchronised hot-wire sensors used for the measurements. For the TBL13k case, one hot wire probe was shifted at various y^+ while the other hot wire probe was maintained at a fixed wall-normal coordinate $y^+ \approx 469$ (corresponding to the centre of the log-layer). Accordingly, a one-point and a two-point AM coefficient can be calculated for TBL13k. In the latter case, $u_L(y_1^+, t)$ and $E_{S,L}(y_2^+, t)$ are shifted in time to get Corr$[u_L(y_1^+, t), u_L(y_2^+, t)]$ maximised (Dogan *et al.* 2019), with $y_1^+ = 3.9\sqrt{Re_*}$ and y_2^+ a wall-normal variable coordinate.

The three turbulent boundary layer datasets used in this study are publicly available online, and further experimental details can be found in previous publications (Baars *et al.* 2015, 2016, 2024).

3. Stochastic thermodynamics approach to AM

The large turbulent scales (u_L) and the small turbulent scale amplitude ($E_{S,L}$) are first discretised using the sign function as $\widetilde{u}_L = \text{Sign}[u_L]$ and $\widetilde{E}_{S,L} = \text{Sign}[E_{S,L}]$. Figure 1(*a*)

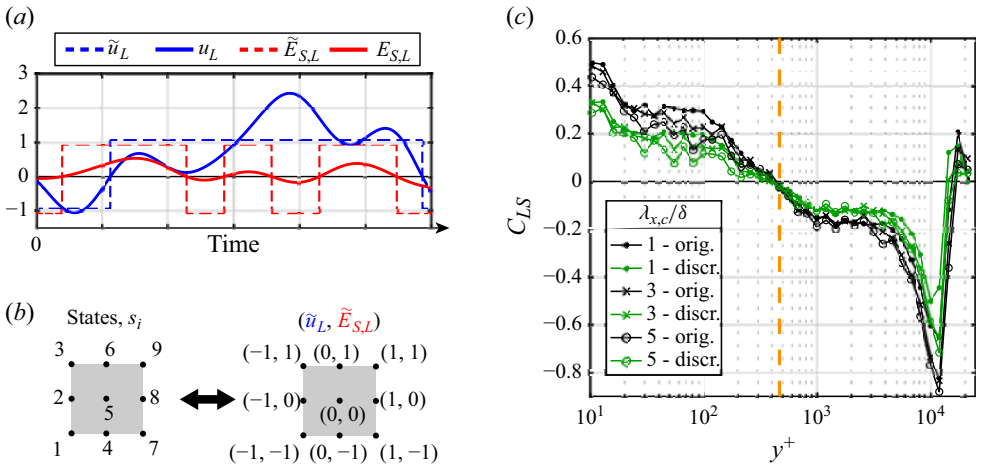

Figure 1. (*a*) Example of u_L and $E_{S,L}$ signals (solid lines) and their discretised versions $\widetilde{u}_L$ and $\widetilde{E}_{S,L}$ (dashed lines). (*b*) States numbering and corresponding pairs of $\widetilde{u}_L$ and $\widetilde{E}_{S,L}$. (*c*) The AM correlation coefficients for the TBL14k case at various cutoff wavelengths $\lambda_{x,co}/\delta$: original signals (black lines) and discretised signals (green lines).

shows an example of u_L and $E_{S,L}$ time series (solid lines) and their discrete counterparts $\widetilde{u}_L$ and $\widetilde{E}_{S,L}$ (dashed lines). A total of $n = 9$ different states, s_i, is obtained where each state corresponds to a pair of discrete values $(\widetilde{u}_L, \widetilde{E}_{S,L})$ as illustrated in figure 1(*b*). Note that $\widetilde{u}_L = 0$ and $\widetilde{E}_{S,L} = 0$ correspond to the nearest time of a zero-crossing of the signals u_L and $E_{S,L}$, respectively.

The sign function represents a simple yet reliable choice for signal discretisation to retain the main features of interscale AM. The validity of our choice is confirmed in figure 1(*c*), which shows the one-point AM coefficient, C_{LS}, obtained from the original (black) and discretised (green) signals for various cutoff filters. Figure 1(*c*) confirms that the key features of the AM phenomenon are preserved after the signal discretisation, specifically, the positive modulation in the near-wall region ($y^+ < 100$) and the sign inversion of the correlation coefficient at $y^+ \approx 3.9\sqrt{Re_*}$ (that is, the wall-normal coordinate of the middle of log-layer (Mathis *et al.* 2009*a*)) are well captured through the discretised signals. It is worth stressing that, the lower correlation values observed after the discretisation are not deemed significant and, most importantly, the dynamical features of the large-small scale coupling behind the AM phenomenon are preserved in $\widetilde{u}_L$ and $\widetilde{E}_{S,L}$. Specifically, the alternating sequence of positive and negative u_L and $E_{S,L}$ values is maintained, as also highlighted in the cross-correlation patterns discussed below (see § 4.3).

The interplay between $\widetilde{u}_L$ and $\widetilde{E}_{S,L}$ is modelled as a Markovian stochastic system on a network of the $n = 9$ states, where the transition probability rate from a state s_j to a state $s_i \neq s_j$ is $r_{ij} \geqslant 0$ (Seifert 2012). Using transition probability rates r_{ij} between states s_i and s_j, a transition rate matrix $\boldsymbol{R} \equiv R_{ij}$ is constructed as $R_{ij} = r_{ij}$ if $i \neq j$, and $R_{ii} = -\sum_k r_{ki}$ for any $k \neq i$. The dynamics of the marginal probability distribution for each state $\boldsymbol{p} \equiv p(s_i)$ therefore follows the master equation $\mathrm{d}\boldsymbol{p}/\mathrm{d}t = \boldsymbol{R}\,\boldsymbol{p}$ (Andrieux & Gaspard 2007; Seifert 2012; Ohga *et al.* 2023). By using this transition network model, Schnakenberg's network theory can be applied, where the vertices of a network correspond to the states of the stochastic system, while edges are transition probabilities between such states (Schnakenberg 1976; Andrieux & Gaspard 2007). Particularly, Schnakenberg found that the system entropy generation can be expressed at a macroscopic level in terms of

network cycles (Schnakenberg 1976). A key quantity in Schnakenberg's theory is the cycle affinity, which is defined as

$$\mathcal{F}_c = \sum_{(i,j)\in c} \ln \frac{r_{ij}}{r_{ji}}, \tag{3.1}$$

for each network cycle c with non-repeating states (Seifert 2012). The cycle affinity $\mathcal{F}_c$ quantifies the entropy variation associated with the completion of a cycle c in the steady state, and therefore it vanishes in equilibrium conditions (Schnakenberg 1976; Seifert 2012). Moreover, $\mathcal{F}_c$ is associated with the thermodynamic forces (such as a chemical reaction potential) maintaining the system in non-equilibrium conditions (Andrieux & Gaspard 2007; Seifert 2012).

Using the interpretation of $\mathcal{F}_c$ as entropy production over the completion of a cycle c, the thermodynamic entropy generation rate for all network cycles can be calculated as

$$s_{aff} = \sum_c \mathcal{F}_c (J_{c_+} - J_{c_-}) = \sum_c \mathcal{F}_c \left(\frac{n_{c_+}}{T} - \frac{n_{c_-}}{T} \right), \tag{3.2}$$

where $J_{c_+} = n_{c_+}/T$ and $J_{c_-} = n_{c_-}/T$ are the cycle currents, T is the time-series length and n_{c_+} and n_{c_-} are the number of times a cycle c is completed clockwise and anticlockwise in a time series (Seifert 2012). All entropy terms in this work are intended to be normalised by the Boltzmann constant (Seifert 2012; Falasco & Esposito 2025).

The mean entropy generation rates for the AM process written in terms of both stochastic thermodynamics and fluid dynamics formalisms are expected to agree both qualitatively and quantitatively up to a proportionality factor depending on methodological aspects (e.g. the state discretisation). In fact, the entropy production rate related to a physical phenomenon (turbulence AM, in this case) should be quantifiable using different methods that are able to capture the underlying physical phenomenon. Here we find a strong link between the two formalisms and find that the mean stochastic thermodynamic entropy generation rate associated with network cycles, $\langle s_{aff} \rangle$, is directly proportional to a mean turbulent entropy generation rate associated with the interscale energy transfer, $\langle s_{LS} \rangle$, as

$$\langle s_{LS} \rangle = \alpha \langle s_{aff} \rangle + \beta, \tag{3.3}$$

where β is a residual entropy generation rate, α is a proportionality factor and $\langle \bullet \rangle$ signifies ensemble averaging over N_{ea} signals (see table 1). While a convergence of the wall-normal behaviour of the entropy generation rates is observed for lower N_{ea} (longer signals) as discussed in Appendix C, ensemble averages are taken as different signal samples generate different values of s_{LS} and s_{aff} due to statistical variability in the measurements, although the spread in many cases is not significant (e.g. see error bars in figure 3*a*), thus leading to smoother and more statistically robust results.

The entropy relation in (3.3) connects the stochastic thermodynamics representation of AM in wall turbulence (via s_{aff}) with a fluid mechanics representation of the interscale energy transfer (via s_{LS}). However, while s_{aff} is well defined in stochastic thermodynamics as per (3.2) (Seifert 2012), s_{LS} needs to be determined by means of fluid mechanics arguments. Here, we address this issue and find that (3.3) holds if $\langle s_{LS} \rangle$ is defined as

$$\langle s_{LS} \rangle \equiv \frac{\langle \Delta \Theta_{LS} \rangle}{k_S}, \tag{3.4}$$

where $k_S = \langle u_S^2 \rangle / 2$ is the small-scale kinetic energy acting as a temperature of the system (as proposed by Yao, Zaki & Meneveau 2023) and $\langle \Delta \Theta_{LS} \rangle$ is the net large-to-small scale

streamwise turbulent kinetic energy production (note that, for Ease of notation, angle brackets in $\langle s_{LS}\rangle$ indicate both ensemble and temporal averaging). Particularly, $\langle \Delta\Theta_{LS}\rangle$ is defined as $\langle \Delta\Theta_{LS}\rangle \equiv \langle \Theta_S\rangle - \langle \Theta_L\rangle$, where $\langle \Theta_S\rangle$ and $\langle \Theta_L\rangle$ are (Kawata & Alfredsson 2018)

$$\langle \Theta_S\rangle = -2\left\langle u_S u_S \frac{\partial u_L}{\partial x}\right\rangle, \quad \langle \Theta_L\rangle = 2\left\langle u_L u_L \frac{\partial u_S}{\partial x}\right\rangle, \tag{3.5}$$

with spatial derivatives are calculated by invoking again Taylor's hypothesis, $\mathrm{d}x = -U(y)\,\mathrm{d}t$. The two terms $\langle \Theta_S\rangle$ and $\langle \Theta_L\rangle$ have the form of energy production terms and have been interpreted as the energy transfer from the large to small scales ($\langle \Theta_S\rangle$), and *vice versa* ($\langle \Theta_L\rangle$) (Kawata & Alfredsson 2018; Chan, Schlatter & Chin 2021). Both $\langle \Theta_S\rangle$ and $\langle \Theta_L\rangle$ are positive quantities indicating that energy is mainly transferred from the large to the small scales (Wang *et al.* 2021). However, $\langle \Theta_S\rangle$ and $\langle \Theta_L\rangle$ can have different values due to the different quantities involved: the former represents the rate of energy due to large-scale internal shear layers ($\partial u_L/\partial x$), while the latter represents the rate of energy due to the small-scale internal shear layers ($\partial u_S/\partial x$). The difference between these two quantities, i.e. $\langle \Delta\Theta_{LS}\rangle$, therefore, is referred to here as the net large-to-small scale streamwise turbulent kinetic energy production that, in general, can be either positive or negative depending on the relative magnitude of $\langle \Theta_S\rangle$ and $\langle \Theta_L\rangle$. As discussed in § 4, however, $\langle \Delta\Theta_{LS}\rangle$ is mostly positive throughout the boundary layer height, in the range of cutoff wavelengths considered here.

The expression for $\langle s_{LS}\rangle$ in (3.4) was inspired by Yao *et al.* (2023), where an entropy generation rate is defined in terms of interscale energy transfer in the context of isotropic turbulence and a normalisation of the energy transfer through the small-scale turbulence kinetic energy is proposed. On this point, it is worth noting that, a more rigorous definition of temperature for the system – as well as $\langle \Theta_S\rangle$, $\langle \Theta_L\rangle$ – should involve all three velocity components. Using the streamwise velocity component only, therefore, leads to a simplification that is, however, deemed reasonable in the context of AM in wall turbulence as follows from extensive literature on the AM of the streamwise velocity u (see § 1).

4. Results

Evidence for the applicability of (universal) thermodynamic bounds is first reported in § 4.1. We then show the validity of (3.3) for the three datasets in § 4.2. Further insights into the small- and large-scale arrangement are also discussed in § 4.3.

4.1. *Verification of universal thermodynamic bounds in wall turbulence*

Thermodynamic bounds have been found to apply to various physical systems (Nicholson *et al.* 2020), such as in biological systems (Ohga *et al.* 2023). Equivalent bounds holding in turbulence, however, are rarer (Tanogami & Araki 2024). In this article, we show that the thermodynamic bounds derived by Ohga *et al.* (2023) are verified in turbulent boundary layer flows. For a Markov (stochastic) model like the one described in § 3, the following inequalities are expected to hold:

$$|\chi_{ba}| \leqslant \underbrace{\max_c \frac{\tanh\left[\mathcal{F}_c/(2n_c)\right]}{\tan(\pi/n_c)}}_{\mathcal{F}_{up}} \leqslant \underbrace{\max_c \frac{\mathcal{F}_c}{2\pi}}_{\mathcal{F}_\infty}, \tag{4.1}$$

where c is a cycle of $n_c \geqslant 3$ non-repeating states (where n_c is the number of states in the cycle) (Ohga *et al.* 2023). The quantity on the left-hand side of (4.1), χ_{ba}, is a measure of

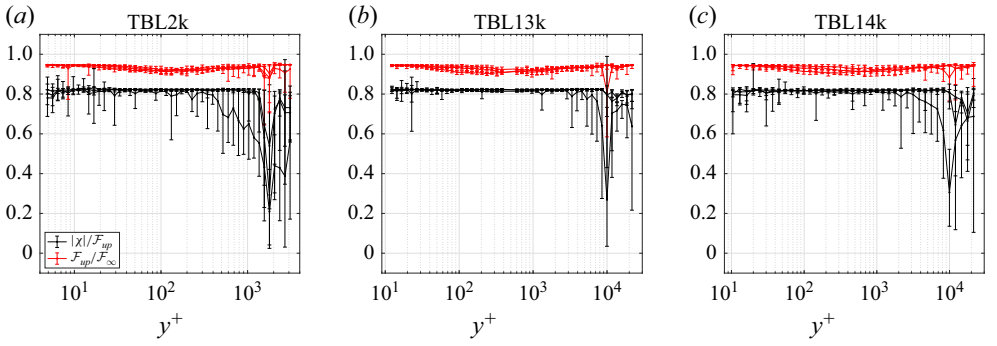

Figure 2. The inequalities in (4.1) are reported for the three experimental datasets as a function of y^+, and at various cutoff wavelengths: $\lambda_{x,co}/\delta = 1$, $\lambda_{x,co}/\delta = 3$ and $\lambda_{x,co}/\delta = 5$. Since the effect of $\lambda_{x,co}$ is not discernible due to overlapping, the same colour and marker symbol are used for the three cutoff thresholds, $\lambda_{x,co}$. Panel (*b*) includes both one- and two-point results. Black plots correspond to $|\chi_{ba}|/\mathcal{F}_{up}$ while red plots correspond to the ratio $\mathcal{F}_{up}/\mathcal{F}_\infty$. The mean values are shown with error bars representing the minimum and maximum values for each ratio at various y^+.

correlation asymmetry, defined as

$$\chi_{ba} = \lim_{\tau \to 0} \frac{C^\tau_{ba} - C^\tau_{ab}}{2\sqrt{\left(C^0_{aa} - C^\tau_{aa}\right)\left(C^0_{bb} - C^\tau_{bb}\right)}}, \tag{4.2}$$

where $C^\tau_{ba} = \mathrm{Corr}[b(t+\tau), a(t)]$ and $C^\tau_{ab} = \mathrm{Corr}[a(t+\tau), b(t)]$ are the two-time cross-correlations between variables a and b at time lag τ, and C^τ_{aa} and C^τ_{bb} are autocorrelations (Ohga *et al.* 2023). In this study, $a(t) \equiv \widetilde{u}_L(t)$ and $b(t) \equiv \widetilde{E}_{S,L}(t)$. The asymmetry $C^\tau_{ba} \neq C^\tau_{ab}$ is a fundamental statistical signature of systems in non-equilibrium steady state (Ohga *et al.* 2023).

Equation (4.1) implies that $|\chi_{ba}|/\mathcal{F}_{up} \leqslant 1$ (tighter bound) and $\mathcal{F}_{up}/\mathcal{F}_\infty \leqslant 1$, which are verified in figure 2 for all datasets, at all wall-normal location y^+, at all cutoff wavelengths $\lambda_{x,co}$ used to decompose small- and large-scales, and for both one-point and two-point AM. A noisy behaviour is observed in the intermittency region, namely, for $y/\delta \to 1$, where AM is not expected to occur (Mathis *et al.* 2009*a*); nevertheless, thermodynamic bounds are still verified in the intermittency region.

Figure 2 shows that thermodynamic bounds hold for the AM interaction (question (ii)), and provides *a posteriori* evidence on the applicability of the discrete stochastic Markov model and Schnakenberg's cycle representation of AM in wall turbulence. Most notably, while such thermodynamic bounds have been proved to hold for discrete-state systems, the extension to continuous-state systems such as turbulence was left to be proved by Ohga *et al.* (2023). Here we provide evidence that the thermodynamic bounds in (4.1) hold for continuous-state systems, provided that a suitable time-series discretisation is performed that captures the system dynamics (figure 1*c*).

Besides the inequalities verification, it is worth highlighting that χ_{ba} can be interpreted as a measure of directed information flow from variable a to variable b (Ohga *et al.* 2023), namely, from the large scales to the small scales in this study. In other words, χ_{ba} can be seen as a measure of the extent to which information of large-scale motion is transferred to small scales (Tanogami & Araki 2024). The inequalities in (4.1), therefore, indicate that large-to-small-scale information flow is bounded by the cycle affinity. Using the analogy between $\mathcal{F}_c$ and $\Delta\Theta_{LS}$ as discussed in § 4.2 below, inequalities in (4.1) suggest – like in other systems in non-equilibrium steady state such as biochemical systems

(Mehta & Schwab 2012) – the presence of thermodynamic trade-offs on the information flow that can be achieved for a given interscale energy production level $\Delta\Theta_{LS}$ and kinetic energy k_S.

It follows that a possible interpretation for these ratios is of information-thermodynamic efficiency, namely, how efficiently information flows from large-scales to small-scales (Tanogami & Araki 2024). Figure 2 shows that the inequality ratios – hence information-thermodynamic efficiency – are largely uniform across the boundary layer, although both $|\chi_{ba}|$ and $\mathcal{F}_{up}$ (or $\mathcal{F}_\infty$) are not constant with y^+ (not shown). Further results on the inequality verification are also provided in Appendix A using a different choice for the convection velocity. Interestingly, the inequality ratios tend to decrease in the near-wall region for $U_{conv} = u'$, suggesting that the interscale information flow (χ_{ba}) is lower compared with the corresponding upper bounds, namely, a lower information-thermodynamic efficiency. Explaining such a difference for the two choices of U_{conv} requires a deeper understanding of the relation between χ_{ba} and the cycle affinity $\mathcal{F}_c$ proposed by Ohga *et al.* (2023), both from a stochastic thermodynamics and fluid mechanics perspectives; however, this is outside the scope of this work and will be explored in future studies.

4.2. *Equivalence of mean entropy production rates*

To visually demonstrate the validity of the equivalence relation between entropies in (3.3), the wall-normal behaviour of the entropies normalised in wall units – namely, $\langle s^+_{LS}\rangle = \langle s_{LS}\rangle t_*$ and $\langle s^+\rangle_{fit} = \alpha_{fit}\langle s^+_{aff}\rangle + \beta_{fit}$, where $\langle s^+_{aff}\rangle = \langle s_{aff}\rangle t_*$ and $t_* = \nu/U_*^2$ is the wall-unit time scale – is shown in figure 3(a) for the TBL14k case. The proportionality parameters, α_{fit} and β_{fit}, are obtained through linear fitting between $\langle s_{LS}(y)\rangle$ and $\langle s_{aff}(y)\rangle$. Two fitting ranges are used, namely, $y/\delta \leqslant 0.5$ and $y/\delta \leqslant 0.8$ (vertical dashed lines in figure 3a): the former value corresponds to the wall-normal location where the intermittent region starts (Baars *et al.* 2015), while the latter value extends the fitting range but keeping it lower than unity to discard the highly intermittent region for $y/\delta \to 1$.

Figure 3(a) clearly indicates a very good overlap for various cutoff wavelengths. In particular, figure 3(a) shows that $\langle s^+_{LS}\rangle > 0$ throughout the boundary layer, i.e. $\langle \Theta_S\rangle > \langle \Theta_L\rangle$. Interestingly, the entropy generation rate has a maximum in the log layer, shifting to higher y^+ by increasing the cutoff wavelength $\lambda_{x,co}$. This outcome was not visible from a simple cross-correlation analysis as shown in figure 1(c), and it points out that the peak entropy generation rate resides in the log layer rather than in the buffer layer, as one might have expected as the buffer layer hosts several key dynamical phenomena in wall turbulence (Jiménez 2018). Since the entropy production rate can be seen as a measure of the power consumed by a system in maintaining the non-equilibrium steady state (Mehta & Schwab 2012), figure 3(a) (as well as results reported in Appendix C) indicates that the log layer is the region where most of the power is needed to maintain the non-equilibrium steady state between large and small velocity scales involved in the AM mechanism. This outcome can be explained as a result of the more significant degree of misalignment between large- and small-scale velocities in the log layer, which can be observed, e.g. from the lagged cross-correlation patterns as shown in figure 4.

A more quantitative analysis of (3.3) is performed to obtain the parameters α and β. Starting from the latter, the residual entropy generation rate β is shown in figure 3(b) as a percentage of $\overline{\langle s_{LS}\rangle}$, with $\overline{\bullet}$ indicating averaging over y. Since β is a scalar, it accounts for the whole variations along the wall-normal direction and, therefore, percentages need to be interpreted as a ratio over the whole boundary layer height. The parameter β can be interpreted as $\beta \equiv \overline{\langle s_{res,aff}\rangle} - \overline{\langle s_{res,LS}\rangle}$, where $s_{res,aff}$ includes the residual entropy not associated with cycles, and $s_{res,LS}$ includes the residual entropy not associated with

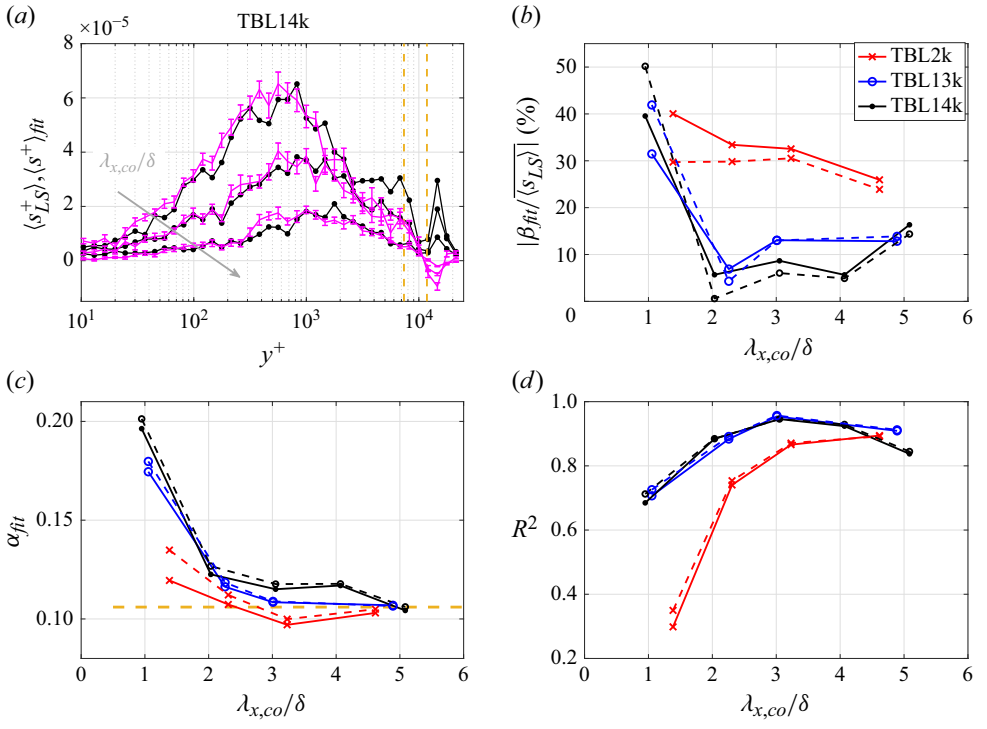

Figure 3. (*a*) Wall-normal behaviour of $\langle s^+_{LS}\rangle$ (magenta lines) and $\langle s^+\rangle_{fit}$ (black lines) for $\lambda_{x,co}/\delta = 2, 3, 5$; error bars indicate the standard error of the mean. The vertical dashed lines are $y/\delta = 0.5$ and $y/\delta = 0.8$. (*b*) Wall-normal behaviour of $|\beta_{fit}/\overline{\langle s_{LS}\rangle}|$ as a percentage. (*c*) Wall-normal behaviour of α_{fit} and (*d*) the goodness of fit R^2. In panels (*b–d*), solid lines correspond to fitting up to $y/\delta = 0.5$ while dashed lines to $y/\delta = 0.8$, and the same colour legend as in (*b*) applies to (*c*) and (*d*). The horizontal dashed line in (*c*) is $\alpha = 0.106$.

local energy transfer such as due to spatial transport. Figure 3(*b*) reveals that β_{fit} is a small fraction of $\overline{\langle s_{LS}\rangle}$ for $\lambda_{x,co}/\delta \geqslant 2$ at high Reynolds number (TBL13k and TBL14k). Higher percentage values are found for the TBL2k case as expected because AM is less enhanced at a lower Reynolds number (Mathis *et al.* 2009*a*), suggesting that residual terms contribute more significantly to the entropy generation rate associated with the AM phenomenon. This is in agreement with previous studies showing that $\langle \Theta_S\rangle$ and $\langle \Theta_L\rangle$ are weaker at lower Reynolds numbers (Wang *et al.* 2021), thereby suggesting that their contribution – and in turn the contribution of $\langle \Delta\Theta_{LS}\rangle$ in $\langle s_{LS}\rangle$ – in the AM mechanisms reduces as Re_* decreases. Moreover, the larger values of β for $\lambda_{x,co}/\delta = 1$ in figure 3(*b*) are associated with the fact that $\langle s_{LS}\rangle$ drops towards the edge of the boundary layer (this can be observed in figures 10*d*, 11*d* and 12*d*; see Appendix C), thus leading to poorer fitting (figure 3*d*). However, the near-wall behaviours of $\langle s_{LS}\rangle$ and $\langle s_{aff}\rangle$ are still in agreement, as well as the wall-normal location of their peak (see figures 10*a*,*d*, 11*a*,*d* and 12*a*,*d*).

The behaviour of α_{fit} and the goodness-of-fit parameter, R^2 (also known as the coefficient of determination), are shown in figure 3(*c–d*). The goodness-of-fit parameter R^2 reaches high values (larger than 0.9) as the cutoff filter increases, quantitatively confirming the high degree of overlap illustrated in figure 3(*a*). In particular, the highest R^2 is observed at approximately $\lambda_{x,co}/\delta \approx 3$, as at this threshold small- and large-scale velocity are well separated (this is more evident at higher Reynolds number due to the larger spectral separation). Similar to β_{fit}, the slope coefficient α_{fit} also tends to converge

for $\lambda_{x,co}/\delta \geqslant 2$, providing a unique estimate for high-Re_* turbulent boundary layers of $\alpha_{fit} \approx 0.106$ (dashed horizontal line in figure 3*c*). As shown in figure 3(*b–d*), the fitting range does not significantly affect the results, especially in terms of the goodness-of-fit parameter (figure 3*d*).

Based on results reported in figure 3, we can conclude that a proportionality relation exists between the entropy generation rate written in the fluid mechanics (turbulence) formalism and stochastic thermodynamics formalism, i.e. $\langle s_{LS} \rangle \simeq \alpha \langle s_{aff} \rangle$. Combining this outcome with the observation that one specific cycle, $\widehat{c}_+ \equiv \{1; 2; 3; 6; 9; 8; 7; 4; 1\}$, is found as the most likely to occur at all vertical coordinates y^+ (see cycle occurrence analysis in Appendix B), (3.3) can be rewritten as

$$\langle s_{LS} \rangle = \frac{\langle \Delta \Theta_{LS} \rangle}{k_S} \sim \left\langle \mathcal{F}_{\widehat{c}} \left(J_{\widehat{c}_+} - J_{\widehat{c}_-} \right) \right\rangle, \tag{4.3}$$

for $y/\delta < 0.8$ (where $\widehat{c}_-$ refers to reversed cycle, i.e. $\widehat{c}_+$ taken in the reversed order). Equation (4.3) indicates that the behaviour of $\langle s_{LS} \rangle$ is proportionally related to the affinity and occurrence of the cycle $\widehat{c}$ (taken in the clockwise or anticlockwise direction); further discussion on cycle $\widehat{c}$ and its relation to large-small scale arrangement is provided in § 4.3. Recalling the thermodynamic interpretation of cycle affinity $\mathcal{F}_c$ (§ 3), results discussed in this section and presented in figure 3 suggest that net large-to-small scale turbulent kinetic energy production, $\langle \Delta \Theta_{LS} \rangle$, is a candidate turbulence quantity to be interpreted as an analogous thermodynamic force driving the AM process out-of-equilibrium (question (i)) for $1 < \lambda_{x,co}/\delta < 5$. Although further research is needed to establish a direct relationship between the two formalisms, present results provide further evidence of an interdisciplinary link between turbulence and stochastic thermodynamics.

4.3. *Large-small scale arrangement*

As mentioned in the previous section and as reported in Appendix B, the discretisation of the AM dynamics into nine states leads to the emergence of the cycle $\widehat{c}_+ \equiv \{1; 2; 3; 6; 9; 8; 7; 4; 1\}$ and its reversed $\widehat{c}_- \equiv \{1; 4; 7; 8; 9; 6; 3; 2; 1\}$ as the most frequent cycles at all y^+. In particular, the cycle $\widehat{c}_+$ is more frequent than $\widehat{c}_-$ at all y^+ (see figure 9 in Appendix B), namely $n_{\widehat{c}_+} > n_{\widehat{c}_-}$. Since $\widehat{c}_+$ is a clockwise cycle (see figure 1*b*), $n_{\widehat{c}_+} > n_{\widehat{c}_-}$ implies that the small-scale velocity amplitude, $\widetilde{E}_{S,L}$, leads in time (lags in space) the amplitude of $\widetilde{u}_L$ at all y^+. This outcome contrasts previous AM results reporting, through a cross-correlation analysis, a small-scale temporal lead only close to the wall, while a switched behaviour occurs away from the wall (Baars *et al.* 2015, 2017).

The lagged cross-correlation is exemplified in figure 4 for TBL14k for three cutoff wavelengths, and for both the original ($E_{S,L}(t)$ and $u_L(t)$) and discredited ($\widetilde{E}_{S,L}(t)$ and $\widetilde{u}_L(t)$) signals. As shown in figure 4, the lag-lead patterns are preserved in the lagged cross-correlation of the discretised signals (dotted lines) compared with the original signals (solid lines). This indicates that the discrepancy with the literature in terms of large-small scale lag is not due to the signal discretisation operation. The reason for the mismatch with previous studies, instead, is found in the different values of the residence time of each state, namely the amount of time $T(s_i)$ in which each state s_i is observed. Particularly, states can be split into two groups, namely, $\{s_1, s_9\}$ and $\{s_3, s_7\}$, where the former corresponds to the states in which $E_{S,L}(t)$ and $u_L(t)$ are concordant (same sign) while the latter corresponds to states in which $E_{S,L}(t)$ and $u_L(t)$ are discordant (opposite signs), see figure 1(*b*). States involving zero crossings (i.e. $\{s_2, s_4, s_5, s_6, s_8\}$) are not considered here as they do not significantly contribute to the cross-correlation calculations. Accordingly, the fraction of time in which both $E_{S,L}(t)$ and $u_L(t)$ are concordant is indicated as $T(1, 9)/T$ (where

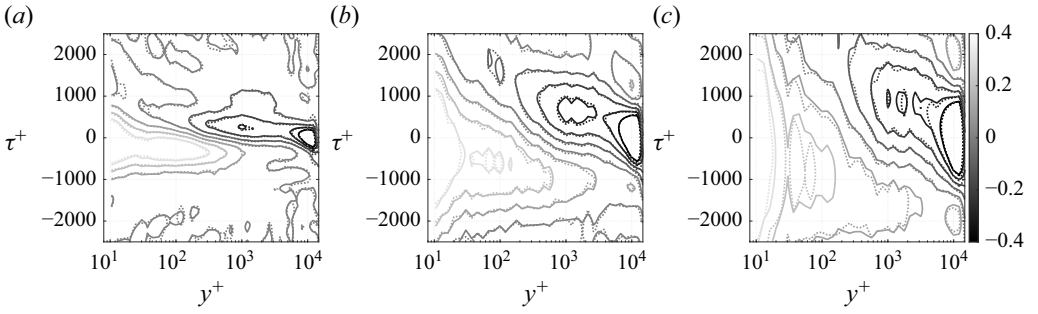

Figure 4. Cross-correlation map between $u_L(t)$ and $E_{S,L}(t)$ (solid lines) and between $\widetilde{u}_L(t)$ and $\widetilde{E}_{S,L}(t)$ (dotted lines) at time lag τ^+ (in wall units), for the TBL14k case at (*a*) $\lambda_{x,co}/\delta = 1$, (*b*) $\lambda_{x,co}/\delta = 3$ and (*c*) $\lambda_{x,co}/\delta = 5$. Isocontours range from -0.4 to 0.4 with a step of 0.1; the same colourbar shown in (*c*) applies to all three panels. For comparison purposes, the discretised cross-correlations (dotted lines) are multiplied by a factor equal to 1.43 in all three panels.

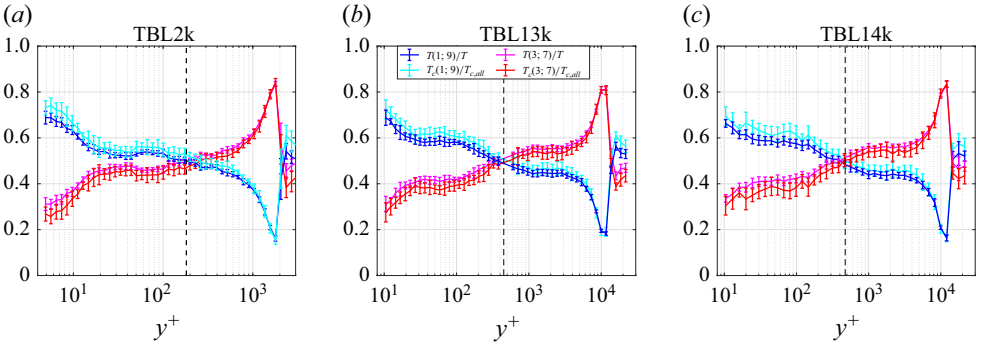

Figure 5. Wall-normal distribution of the fraction of time in which $u_L(t)$ and $E_{S,L}(t)$ are concordant (states 1 and 9) or discordant (states 3 and 7), evaluated at $\lambda_{x,co}/\delta = 3$ for (*a*) TBL2k, (*b*) TBL13k and (*c*) TBL14k. The vertical (black) dashed line is the reference location for the log-layer centre. Here, T_c refers to the residence time calculated for cycles only, and the error bars indicate one standard deviation. The same legend in (*b*) applies to all three panels.

$T(1,9) = T(s_1) + T(s_9)$), while the fraction of time in which both $E_{S,L}(t)$ and $u_L(t)$ are discordant is indicated as $T(3,7)/T$ (where $T(3,7) = T(s_3) + T(s_7)$).

As shown in figure 5, $T(1,9)/T$ (concordant signs) is larger than $T(3,7)/T$ (discordant signs) in the near-wall region, but the two fractions switch above the centre of the log layer (dashed black lines in figure 5). This behaviour is observed not only for the whole time series (blue and magenta lines in figure 5) but also when the time fractions are evaluated for the segments of time series corresponding to all cycles (cyan and red lines in figure 5), i.e. $T_c(1,9)/T_{c,all}$ and $T_c(3,7)/T_{c,all}$, where $T_{c,all}$ is the total amount of time associated with all cycles c. Therefore, the interplay between $\widetilde{E}_{S,L}$ and $\widetilde{u}_L$ is indeed well captured within cyclic intervals of the signals.

Figure 5 reveals that the switch in the lead–lag pattern in the cross-correlation (figure 4) is mainly due to a switch in the duration of temporal intervals in which $E_{S,L}(t)$ and $u_L(t)$ are concordant or discordant. Namely, the switch in the sign of maximum correlation (suggesting a lead or a lag between the two signals) is mainly due to a redistribution of the duration of $T(1,9)$ and $T(3,7)$ in the boundary layer, rather than to variations in the signal amplitudes (note that signals are Z-score normalised in the definition of correlation coefficient). This change is illustrated in figure 6, where residence times are clearly visible

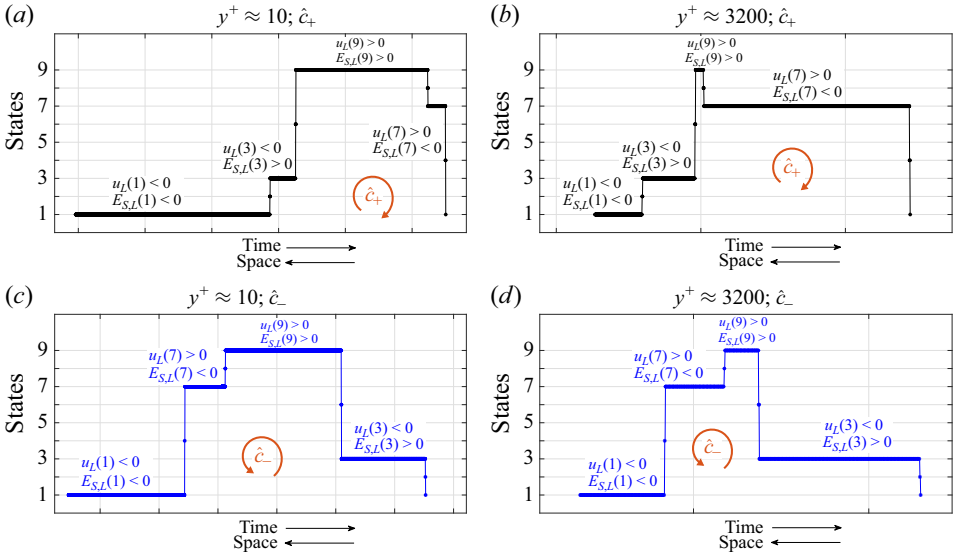

Figure 6. Four examples of discrete state signals extracted from the TBL14k dataset at (*a*,*c*) $y^+ \approx 10$ and (*b*,*d*) $y^+ \approx 3200$. The four intervals highlight the appearance of (*a*,*b*) $\widehat{c}_+$ (clockwise cycle) and (*c*,*d*) $\widehat{c}_-$ (anticlockwise cycle). The corresponding signs of u_L and $E_{S,L}$ are also highlighted, following the state convention of figure 1(*b*). For comparison purposes, the vertical grid spacing is set to the same value for all four plots, equal to $500/f_s$ (where $1/f_s$ is the sampling time step).

within each (clockwise and anticlockwise) cycle, either close to the wall (figure 5*a*,*c*) and above the log-layer centre (figure 5*b*,*d*).

From the outcomes reported in figures 4, 5 and 6, as well as figure 9 in Appendix B, we can conclude that small-scale amplitude, $E_{S,L}(t)$, indeed tends to lead in time (lag in space) large scales, u_L, throughout the boundary layer height as suggested by the cycle occurrence, but the different duration of each state significantly affects the sign of the maxima in the cross-correlation. This result does not invalidate previous arguments on why a positive or negative AM is observed close or away from the wall, respectively (e.g. as discussed in § 4 by Baars, Hutchins & Marusic 2017). However, it points out that – by definition of lead and lag between two signals – variations in the amplitude of the small scales are more likely to take place after (in space) the variations in the large-scale signs (figure 6), where the latter correspond to the alternating sequence of large-scale low and high-speed zones. Physically, this conclusion implies that it is more likely that small scales tend to adapt to changes to the behaviour of large scales, rather than *vice versa,* in agreement with the idea that large scales provide a background flow to locally generate small-scale structures (Wang *et al.* 2021).

5. Discussion and conclusions

Results presented in this article provide evidence for the validity of Schnakenberg's network theory in wall turbulence. Specifically, we shed more light on the energetic mechanisms behind AM, showing that the net large-to-small-scale turbulent kinetic energy production, $\langle \Delta\Theta_{LS} \rangle$, can be seen as the main turbulent quantity driving the AM process out-of-equilibrium (question (i)), hence leading to a predominantly positive entropy generation. Interestingly, we find that $\langle \Delta\Theta_{LS} \rangle = \langle \Theta_S \rangle - \langle \Theta_L \rangle$ is the variable that best capture the (interscale) energy transfer behind AM, rather than the total energy transfer

$\langle \Theta_S \rangle + \langle \Theta_L \rangle$ that appears in the transport equation of the scalewise Reynolds stress equation, as derived by Kawata & Alfredsson (2018). In fact, the total energy transfer appears as a source term in the small-scale Reynolds stress equation, which is in agreement with the fact that both $\langle \Theta_S \rangle$ and $\langle \Theta_L \rangle$ are positive and hence pointing to a prevalent forward energy cascade mechanism (Wang *et al.* 2021). However, in the context of AM, it turns out that the interplay between the energy transfer due to the large-scale velocity gradient ($\langle \Theta_S \rangle$) and the energy transfer due to the small-scale velocity gradient ($\langle \Theta_L \rangle$) is a more appropriate quantity. In particular, $\langle \Theta_S \rangle > \langle \Theta_L \rangle$ is the condition that leads to a positive entropy generation rate (figure 3*a*), which implies that most of the energy transfer can be associated with large-scale velocity gradients (i.e. due to $\partial u_L / \partial x$). This result resonates with previous works, e.g. focusing on conditional analysis, highlighting that the small-scale amplitude changes depending on the large-scale internal shear layer behaviour (Baars *et al.* 2017). Moreover, coherent structures – i.e. low-speed streaks and quasistreamwise vortices, as well as hairpin vortices – have been associated with events of large $\langle \Theta_S \rangle$ and $\langle \Theta_L \rangle$ values (Wang *et al.* 2021), thus supporting the argument for a link between the development of coherent structures and entropy generation and irreversibility (Iacobello *et al.* 2023).

Remarkably, our results are obtained at scale separations ($\lambda_{x,co}$) at least three orders of magnitude larger than dissipative scales, which are of the order of the Kolmogorov length scale, $\eta^+ = O(1)$ (Smits *et al.* 2011), and where thermal fluctuation effects become relevant (Bandak *et al.* 2022; Tanogami & Araki 2024). This outcome supports the argument that stochastic thermodynamics is applicable at scales much larger than the microscopic scale, provided that a sufficient scale separation exists between the slow (large scale) degrees of freedom and the fast (small scale) ones (Seifert 2012). This is indeed the case of wall turbulence at high Reynolds numbers, where a neat large-small scale separation exists between the large- and small-scale motions both in energetic terms and in their temporal evolution (Jiménez 2018).

It is important to remark here that the linear relationship between $\langle s_{LS} \rangle$ and $\langle s_{aff} \rangle$ of (3.3) – as well as (4.3) – is derived on the basis of a similarity process, where the wall-normal behaviour of the two mean entropy generation rates is observed to match for various Reynolds numbers and cutoff wavelengths (see figure 3). Accordingly, (3.3) is to be interpreted as a regression model with fitting parameters α and β. Nevertheless, as discussed above, it is known that many features of the AM in wall turbulence can be associated with the spatiotemporal arrangement of the small and large scales along internal shear layers (Baars *et al.* 2017; Saxton-Fox, Lozano-Durán & McKeon 2022). Therefore, the involvement of $\langle \Theta_S \rangle$ and $\langle \Theta_L \rangle$ (which include spatial derivatives of u_L and u_S) in (3.3) aligns well, from a physical perspective, with the modelling of AM that, in this work, relies on the discrete network representation. These insights, supported by the existence of a robust proportionality relationship between $\langle s_{LS} \rangle$ and $\langle s_{aff} \rangle$ (as discussed in § 4, particularly via the goodness-of-fitting parameter, R^2), suggest the presence of a deeper, more formal, connection between interscale energetic mechanisms in wall-turbulence and the cycle-based, Markovian, representation of the same phenomenon. However, to the best of our knowledge, this formal connection has yet to be established, and future research in this direction would be advocated.

Finally, we speculate that the proposed network model can be extended, for example, to investigate the development of coherent flow structures under a new lens, as these are often identified via thresholding techniques (Kailasnath & Sreenivasan 1993; Wallace 2016; Chowdhuri & Banerjee 2023) naturally leading to a discrete formulation. In this regard, the extension of the present approach to spatial data (e.g. extracted from numerical simulations) is an intriguing and useful aspect connected to the choice of the convection

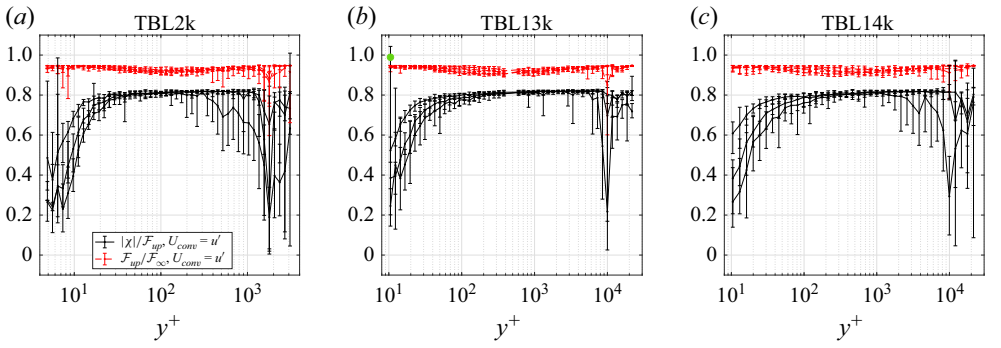

Figure 7. Same as in Figure 2 but for the convection velocity $U_{conv} = u'$. The green marker in (*b*) is $|\chi|/\mathcal{F}_{\infty} < 1$ for the individual signal with $|\chi|/\mathcal{F}_{up} > 1$.

velocity in adopting Taylor's hypothesis (as reported in Appendix A). The extension of the present study to spatial data from numerical simulations is currently under investigation and will be the subject of future work. Moreover, the validity of fluctuation relations in wall turbulence – extending results by Yao *et al.* (2023) – is still an open issue to be explored, as many questions still remain on the connection between turbulence and non-equilibrium thermodynamics (Yao *et al.* 2024). Specifically, the verification of the fluctuation relations requires a robust evaluation of probability distributions, which implies the need for accurately resolved and extensive datasets, alongside appropriate definitions of entropy generation rates. The complementary use of experimental measurements and numerical simulations, therefore, could help shed light on the validity of fluctuation relations in wall turbulence.

Acknowledgements. G.I. would like to thank Professor S. Scarsoglio and Professor L. Ridolfi for their kind and useful feedback on the first manuscript draft, and Professor L. Rondoni for the invaluable conversation on Schnakenberg's network theory at the early stage of this work. G.I. would also like to thank Dr W.J. Baars for the useful comments and acquisition details on the TBL2k dataset. For the purpose of open access, the author has applied a Creative Commons attribution license (CC BY) to any author accepted manuscript version arising from this submission.

Funding. This research received no specific grant from any funding agency, commercial or not-for-profit sectors.

Declaration of interests. The author reports no conflict of interest.

Data availability statement. The three datasets are publicly available online at the following repositories: TBL13k and TBL14k datasets, figshare repository at the University of Melbourne, https://doi.org/10.26188/5e919e62e0dac; TBL2k dataset, SURFdrive repository at https://surfdrive.surf.nl/files/index.php/s/e9h0RqLtvNdDwtj.

Appendix A. Effect of the convection velocity

The choice of the convection velocity, U_{conv}, on the Taylor's hypothesis to convert time series into spatial series is discussed in this appendix. Results reported in the main text correspond to the widely adopted case of $U_{conv} = U(y)$, namely, the convection velocity is the local mean velocity. Here, we show results for $U_{conv} = u'(t, y)$ as proposed by Yang & Howland (2018) in the context of wall turbulence modulation.

Figure 7 shows the inequality ratios (4.1) for the three datasets and at cutoff wavelengths $\lambda_{x,co}/\delta = 1, 3, 5$. Both ratios are smaller than unity, confirming the validity of (4.1). It should be noted that in only one instance the tighter bound $|\chi_{ba}|/\mathcal{F}_{up}$ exceeds unity at the

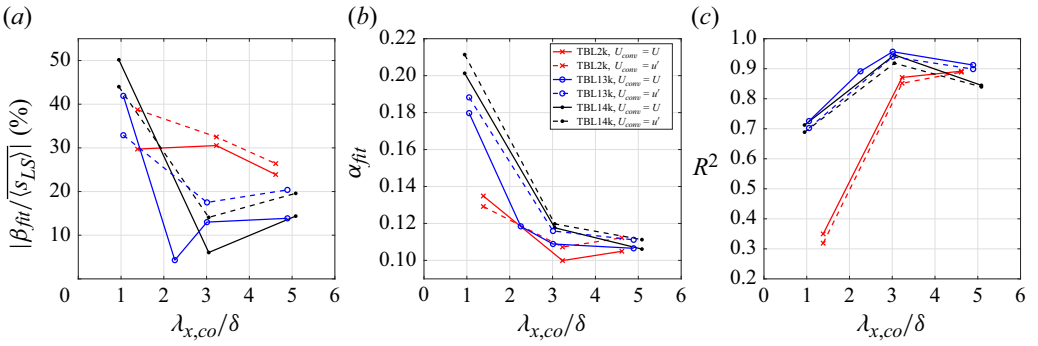

Figure 8. Comparison of the fitting parameters (*a*) β_{fit}, (*b*) α_{fit} and (*c*) the goodness-of-fit parameter R^2 for the two convection velocity definitions, $U_{conv} = U$ (solid lines) and $U_{conv} = u'$ (dashed lines). The fitting range here is $y/\delta < 0.8$. The three datasets are highlighted as: TBL2k, red lines, crosses; TBL13k, blue lines, circles; TBL14k, black lines, filled dots.

first wall-normal location in figure 7(*b*), however, the bound $|\chi_{ba}|/\mathcal{F}_\infty$ is still verified as highlighted by the green marker. This is considered a numerical outlier, which disappears if, for example the time series length is increased.

More generally, it is observed that the ratio $|\chi_{ba}|/\mathcal{F}_{up}$ (black lines) reduces close to the wall ($y^+ < 100$) compared with the reference case, $U_{conv} = U(y)$, shown in figure 2. The reduction in the $|\chi_{ba}|/\mathcal{F}_{up}$ ratio in the near-wall region for $U_{conv} = u'$ indicates that there is a larger gap in the large-to-small-scale information flow for $y^+ < 100$ compared with the log layer, achievable at a given level of affinity $\mathcal{F}$ (i.e. a lower information-thermodynamic efficiency). This near-wall variation in the interscale information-thermodynamic efficiency may be associated with the presence of the wall itself, particularly, with the relationship between the streamwise velocity fluctuations and wall-shear-stress fluctuations in the near-wall region, which was the main argument behind the choice of $U_{conv} = u'(t, y)$ (Yang & Howland 2018). Moreover, efficiency variations in the near-wall region tend to be in agreement with recent observations of a local decoupling between large and small scales in the near-wall region (Andreolli *et al.* 2023). Nevertheless, as already mentioned in § 4.1, additional research is needed to shed more light on the link between χ_{ba} and $\mathcal{F}$ that can explain the behaviour of their ratio.

The impact of the choice of the convection velocity on the analogy of (3.3) is reported in figure 8. Some variations (with respect to the case $U_{conv} = U$; solid lines in figure 8) are noted for the two fitting parameters β_{fit} (figure 8*a*) and α_{fit} (figure 8*b*). However, these variations are not significant, as also emerging from the goodness-of-fit parameter R^2 (figure 8*c*) that closely follow the $U_{conv} = U$ case.

In summary, the results shown in figures 7 and 8 indicate that the proposed stochastic model for AM and the analogy between entropies extend to various choices of the convection velocity.

Appendix B. Wall-normal behaviour of cycle occurrence

The cycle occurrence is evaluated in this appendix, following the cycle decomposition of the network model described in § 3. In particular, we separate the contribution of the cycle $\widehat{c}_+ \equiv \{1; 2; 3; 6; 9; 8; 7; 4; 1\}$ (clockwise), its reversed cycle $\widehat{c}_- \equiv \{1; 4; 7; 8; 9; 6; 3; 2; 1\}$ (anticlockwise), and all the remaining cycles c_{others}. The cycle occurrence is hence defined as the ratio between the number of cycles n_c and the total

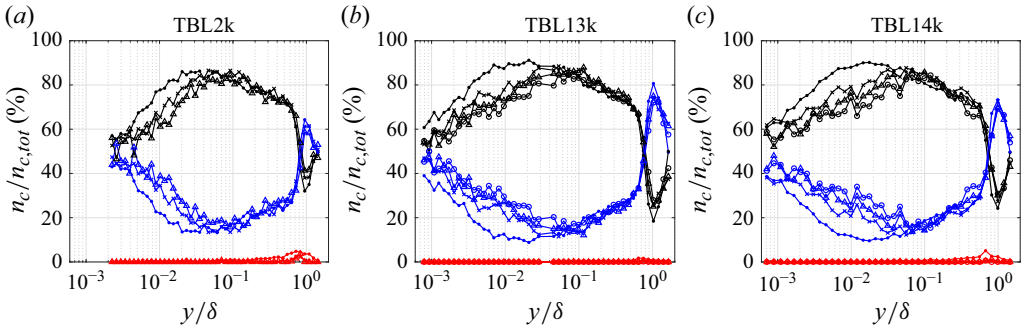

Figure 9. Fraction of the average occurrence of the cycle $\widehat{c}$ occurring in the clockwise direction, $\widehat{c}_+$ (black) and anticlockwise direction, $\widehat{c}_-$ (blue), and all remaining cycles c_{others} (red) as a function of the vertical coordinate, y/δ. The three turbulent boundary layer datasets (TBL2k, TBL13k and TBL14k) are indicated as plot titles. Symbols correspond to various cutoff wavelengths: filled circles, $\lambda_{x,co}/\delta = 1$; crosses, $\lambda_{x,co}/\delta = 3$; open circles, $\lambda_{x,co}/\delta = 5$.

number of cycles:

$$n_{c,tot} = n_{\widehat{c}_+} + n_{\widehat{c}_-} + n_{c_{others}}. \tag{B1}$$

Figure 9 shows the wall-normal distribution (in percentage) of the average $n_c/n_{c,tot}$ ratios for the three datasets, and at various cutoff wavelengths, $\lambda_{x,co}/\delta$ (results are intended to be ensemble averaged but the $\langle\bullet\rangle$ is dropped here only for Ease of notation). It turns out that the cycle $\widehat{c}_+$ and its reversal $\widehat{c}_-$ are the most frequent cycles at all vertical coordinates y (up to the intermittency region), and for all datasets and cutoff wavelengths. Particularly, $\widehat{c}_+$ occurs more frequently on average than $\widehat{c}_-$, as mentioned in § 4.3, supporting the hypothesis that small scales tend to adapt to changes to the behaviour of large scales, rather than *vice versa.*

Appendix C. Parametric analysis on the time series length

The effect of the time series length on the wall-normal behaviour of the entropy production rates, $\langle s_{aff}\rangle$ and $\langle s_{LS}\rangle$, is reported and discussed in this appendix. As reported in table 1 and discussed in § 2, the time series of the streamwise velocity fluctuations $u(y, t)$ are divided into N_{ea} non-overlapping segments of length T. The time series duration T, however, does not provide meaningful information when evaluated in isolation. A more representative value is the T_{min} quantity reported in table 1, that is the minimum ratio between the time series duration T and the temporal length of a turbulent scales with wavelength $\lambda_{x,co}$ advected at the mean velocity U. For a given dataset and a given cutoff wavelength, such a minimum is found for the minimum value of U, which is at the closest point to the wall, y_{min}. An increase in N_{ea}, therefore, results in a decrease in the time series duration compared with the characteristic time scale $\lambda_{x,co}/U$.

The effect of increasing N_{ea}, i.e. decreasing T_{min}, on $\langle s_{aff}\rangle$ and $\langle s_{LS}\rangle$ is illustrated in figures 10, 11 and 12 for the TBL14k, TBL13k and TBL2k cases, respectively. Overall, it turns out that convergence of the results is acceptable for values of T_{min} approximately larger than 40. The results discussed in the main text, however, correspond to a T_{min} largely exceeding this threshold value for all cutoff wavelengths (see blue lines in figures 10, 11 and 12). As expected, the lack of convergence is amplified for larger cutoff values (figures 10*c*, *f*, 11*c*, *f* and 12*c*, *f*) and the measurement points closer to the wall are those more affected by an increase in N_{ea}.

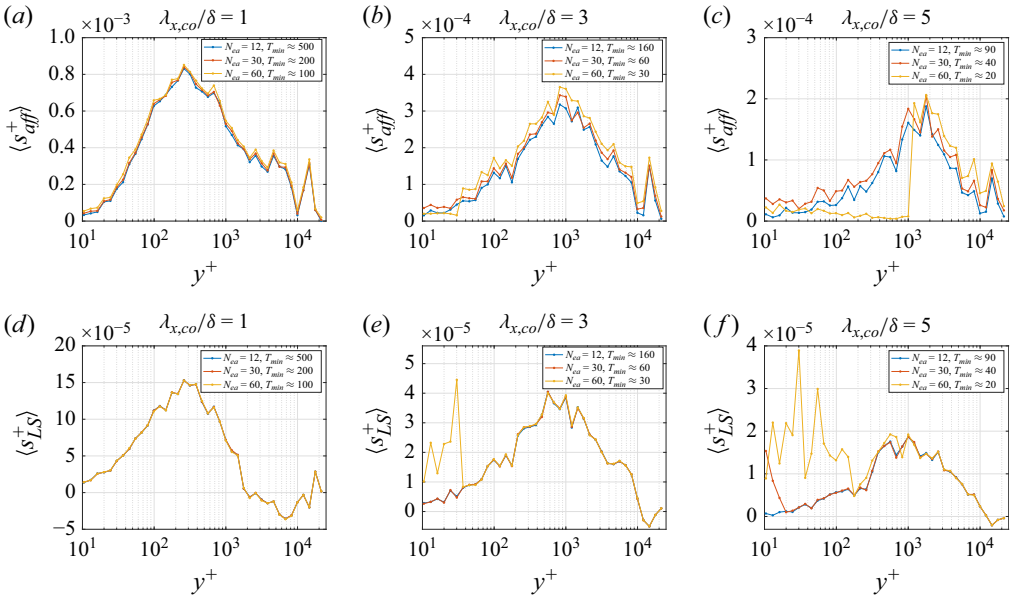

Figure 10. Wall-normal behaviour of (*a–c*) $\langle s_{LS} \rangle$ and (*d–f*) $\langle s_{aff} \rangle$ for increasing values of N_{ea} (decreasing values of T_{min}) for the TBL14k case. The three cutoff wavelengths are (*a*,*d*) $\lambda_{x,co}/\delta = 1$, (*b*,*e*) $\lambda_{x,co}/\delta = 3$ and (*c*,*f*) $\lambda_{x,co}/\delta = 5$.

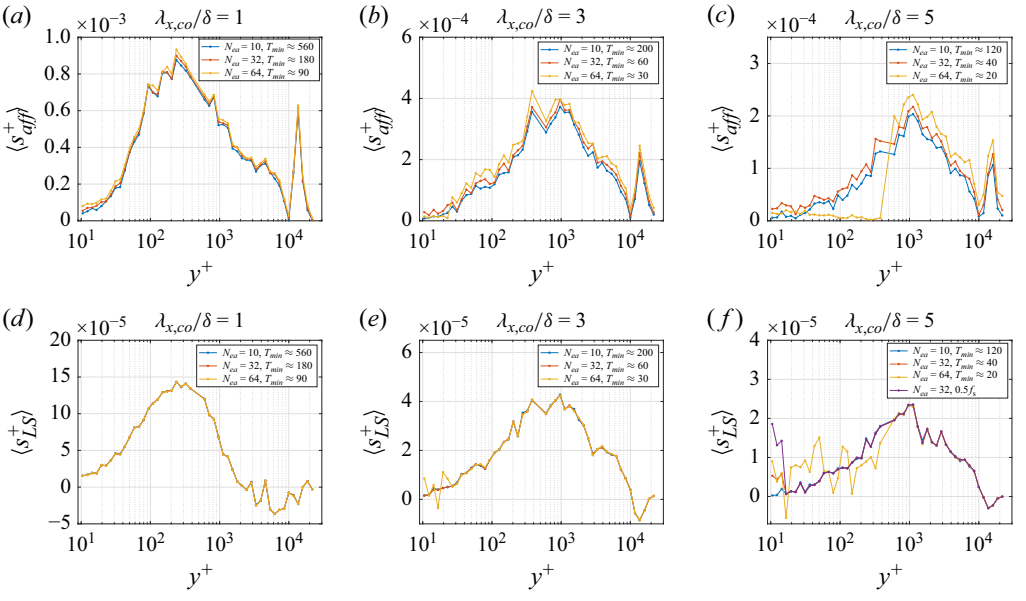

Figure 11. Same as in figure 10 but for the TBL13k case. In (*f*), the purple line corresponds to $N_{ea} = 32$ as for the red line, but where the sampling frequency, f_s, was halved (doubling the sampling time step) to highlight the impact of the sampling frequency at low y^+.

Interestingly, $\langle s_{LS} \rangle$ (figures 10*a–c*, 11*a–c* and 12*a–c*) appears to be more sensitive to an increase in N_{ea} than $\langle s_{aff} \rangle$ (figures 10*d–f*, 11*d–f* and 12*d–f*). This behaviour is mostly associated with border effects (due to the finiteness of the time series) in the calculation of the derivatives $\partial u_L/\partial x$ and $\partial u_S/\partial x$ in (3.5). Moreover, $\langle s_{LS} \rangle$ for the TBL14k case are

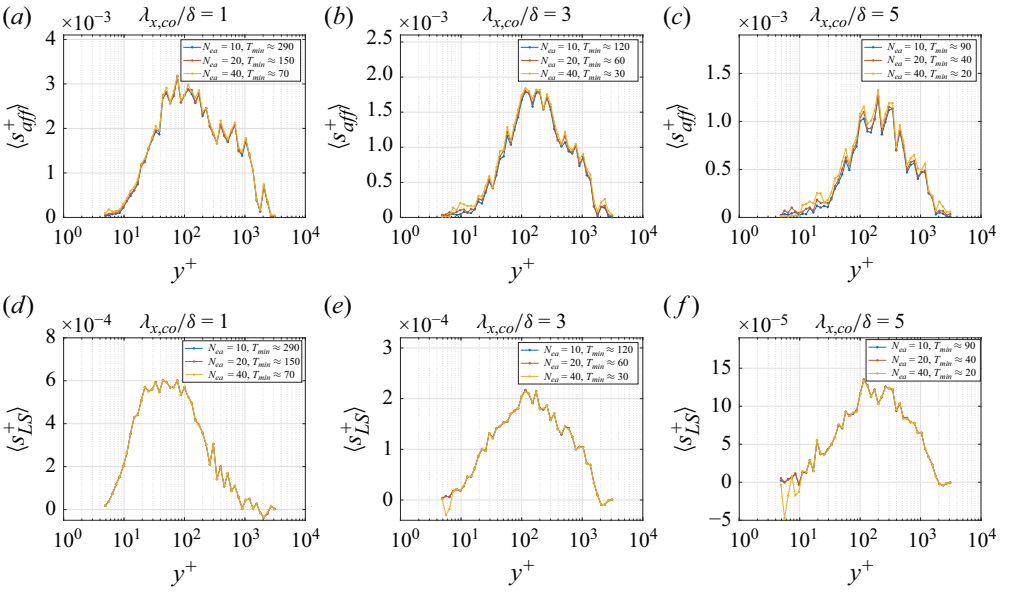

Figure 12. Same as in figure 10 but for the TBL2k case.

more sensitive to an increase in N_{ea} at large cutoff wavelengths (figure 10*e*,*f*) compared with $\langle s_{LS} \rangle$ for the TBL13k case (figure 11*e*, *f*). The reason for this difference – although the Reynolds number values for the two datasets are relatively close – stems from the higher sampling frequency, f_s, of the TBL13k dataset (see table 1), which in turn affect the robustness of the calculation of the derivatives in (3.5). This effect is demonstrated in figure 11(*f*), where the sampling frequency was halved for the $N_{ea} = 32$ case (purple line), resulting in larger deviations of $\langle s_{LS} \rangle$ at small y^+ compared with the case at higher sampling frequency (red line).

In summary, the parametric analysis reported in this appendix points out that results discussed in the main text (corresponding to blue lines in figures 10, 11, 12) are not significantly affected by the time series length (as well as the sampling frequency), for all cutoff wavelengths considered.

References

Agostini, L. & Leschziner, M. 2014 On the influence of outer large-scale structures on near-wall turbulence in channel flow. *Phys. Fluids* **26** (7), 075107.

Anderson, W. 2016 Amplitude modulation of streamwise velocity fluctuations in the roughness sublayer: evidence from large-eddy simulations. *J. Fluid Mech.* **789**, 567–588.

Andreolli, A., Gatti, D., Vinuesa, R., Örlü, R. & Schlatter, P. 2023 Separating large-scale superposition and modulation in turbulent channels. *J. Fluid Mech.* **958**, A37.

Andrieux, D. & Gaspard, P. 2007 Fluctuation theorem for currents and Schnakenberg network theory. *J. Stat. Phys.* **127**, 107–131.

Baars, W.J., Talluru, K.M., Hutchins, N. & Marusic, I. 2015 Wavelet analysis of wall turbulence to study large-scale modulation of small scales. *Exp. Fluids* **56** (10), 188.

Baars, W.J., Dacome, G. & Lee, M. 2024 Reynolds-number scaling of wall-pressure–velocity correlations in wall-bounded turbulence. *J. Fluid Mech.* **981**, A15.

Baars, W.J., Hutchins, N. & Marusic, I. 2016 Spectral stochastic estimation of high-Reynolds-number wall-bounded turbulence for a refined inner-outer interaction model. *Phys. Rev. Fluids* **1** (5), 054406.

Baars, W.J., Hutchins, N. & Marusic, I. 2017 Reynolds number trend of hierarchies and scale interactions in turbulent boundary layers. *Phil. Trans. R. Soc. Lond. A: Math. Phys. Engng Sci.* **375** (2089), 20160077.

BANDAK, D., GOLDENFELD, N., MAILYBAEV, A.A. & EYINK, G. 2022 Dissipation-range fluid turbulence and thermal noise. *Phys. Rev. E* **105** (6), 065113.

CHAN, C.I., SCHLATTER, P. & CHIN, R.C. 2021 Interscale transport mechanisms in turbulent boundary layers. *J. Fluid Mech.* **921**, A13.

CHEMINET, A. *et al.* 2022 Eulerian vs Lagrangian irreversibility in an experimental turbulent swirling flow. *Phys. Rev. Lett.* **129** (12), 124501.

CHOWDHURI, S. & BANERJEE, T. 2023 Revisiting 'bursts' in wall-bounded turbulent flows. *Phys. Rev. Fluids* **8** (4), 044606.

CILIBERTO, S., GARNIER, N., HERNANDEZ, S., LACPATIA, C., PINTON, J. & CHAVARRIA, R. 2004 Experimental test of the Gallavotti–Cohen fluctuation theorem in turbulent flows. *Physica A* **340** (1–3), 240–250.

DOGAN, E., ÖRLÜ, R., GATTI, D., VINUESA, R. & SCHLATTER, P. 2019 Quantification of amplitude modulation in wall-bounded turbulence. *Fluid Dyn. Res.* **51** (1), 011408.

DRIVAS, T.D. 2019 Turbulent cascade direction and Lagrangian time-asymmetry. *J. Nonlinear Sci.* **29** (1), 65–88.

DUVVURI, S. & MCKEON, B.J. 2015 Triadic scale interactions in a turbulent boundary layer. *J. Fluid Mech.* **767**, R4.

EVANS, D.J., COHEN, E.G.D. & MORRISS, G.P. 1993 Probability of second law violations in shearing steady states. *Phys. Rev. Lett.* **71** (15), 2401.

FALASCO, G. & ESPOSITO, M. 2025 Macroscopic stochastic thermodynamics. *Rev. Mod. Phys.* **97** (1), 015002.

FRIEDRICH, R. & PEINKE, J. 1997 Description of a turbulent cascade by a Fokker–Planck equation. *Phys. Rev. Lett.* **78** (5), 863.

FUCHS, A., QUEIRÓS, S.M.D., LIND, P.G., GIRARD, A., BOUCHET, F., WÄCHTER, M. & PEINKE, J. 2020 Small scale structures of turbulence in terms of entropy and fluctuation theorems. *Phys. Rev. Fluids* **5** (3), 034602.

GANAPATHISUBRAMANI, B., HUTCHINS, N., MONTY, J.P., CHUNG, D. & MARUSIC, I. 2012 Amplitude and frequency modulation in wall turbulence. *J. Fluid Mech.* **712** (61), 064602–064617.

HUTCHINS, N. & MARUSIC, I. 2007 Large-scale influences in near-wall turbulence. *Phil. Trans. R. Soc. Lond. A: Math. Phys. Engng Sci.* **365** (1852), 647–664.

IACOBELLO, G., CHOWDHURI, S., RIDOLFI, L., RONDONI, L. & SCARSOGLIO, S. 2023 Coherent structures at the origin of time irreversibility in wall turbulence. *Commun. Phys.* **6** (1), 91.

IACOBELLO, G., RIDOLFI, L. & SCARSOGLIO, S. 2021 Large-to-small scale frequency modulation analysis in wall-bounded turbulence via visibility networks. *J. Fluid Mech.* **918**, A13.

JACHENS, A., SCHUMACHER, J., ECKHARDT, B., KNOBLOCH, K. & FERNHOLZ, H.H. 2006 Asymmetry of temporal cross-correlations in turbulent shear flows. *J. Fluid Mech.* **547**, 55–64.

JIMÉNEZ, J. 2018 Coherent structures in wall-bounded turbulence. *J. Fluid Mech.* **842**, P1.

JUCHA, J., XU, H., PUMIR, A. & BODENSCHATZ, E. 2014 Time-reversal-symmetry breaking in turbulence. *Phys. Rev. Lett.* **113** (5), 054501.

KAILASNATH, P. & SREENIVASAN, K.R. 1993 Zero crossings of velocity fluctuations in turbulent boundary layers. *Phys. Fluids A* **5** (11), 2879–2885.

KAWATA, T. & ALFREDSSON, P.H. 2018 Inverse interscale transport of the Reynolds shear stress in plane Couette turbulence. *Phys. Rev. Lett.* **120** (24), 244501.

MARUSIC, I., CHANDRAN, D., ROUHI, A., FU, M.K., WINE, D., HOLLOWAY, B., CHUNG, D. & SMITS, A.J. 2021 An energy-efficient pathway to turbulent drag reduction. *Nat. Commun.* **12** (1), 5805.

MARUSIC, I., MATHIS, R. & HUTCHINS, N. 2010 Predictive model for wall-bounded turbulent flow. *Science* **329** (5988), 193–196.

MATHIS, R., HUTCHINS, N. & MARUSIC, I. 2009*a* Large-scale amplitude modulation of the small-scale structures in turbulent boundary layers. *J. Fluid Mech.* **628**, 311–337.

MATHIS, R., MONTY, J.P., HUTCHINS, N. & MARUSIC, I. 2009*b* Comparison of large-scale amplitude modulation in turbulent boundary layers, pipes, and channel flows. *Phys. Fluids* **21** (11), 111703.

MEHTA, P. & SCHWAB, D.J. 2012 Energetic costs of cellular computation. *Proc. Natl Acad. Sci. USA* **109** (44), 17978–17982.

NICHOLSON, S.B., GARCÍA-PINTOS, L.P., DEL CAMPO, A. & GREEN, J.R. 2020 Time–information uncertainty relations in thermodynamics. *Nat. Phys.* **16** (12), 1211–1215.

NICKELSEN, D. & ENGEL, A. 2013 Probing small-scale intermittency with a fluctuation theorem. *Phys. Rev. Lett.* **110** (21), 214501.

OHGA, N., ITO, S. & KOLCHINSKY, A. 2023 Thermodynamic bound on the asymmetry of cross-correlations. *Phys. Rev. Lett.* **131** (7), 077101.

PEINKE, J., TABAR, M.R. & WÄCHTER, M. 2019 The Fokker–Planck approach to complex spatiotemporal disordered systems. *Annu. Rev. Condens. Matt. Phys.* **10**, 107–132.
POLANCO, J.I., VINKOVIC, I., STELZENMULLER, N., MORDANT, N. & BOURGOIN, M. 2018 Relative dispersion of particle pairs in turbulent channel flow. *Intl J. Heat Fluid Flow* **71**, 231–245.
PORPORATO, A., HOOSHYAR, M., BRAGG, A.D. & KATUL, G. 2020 Fluctuation theorem and extended thermodynamics of turbulence. *Proc. R. Soc. Lond. A: Math. Phys. Engng Sci.* **476** (2243), 20200468.
REINKE, N., FUCHS, A., NICKELSEN, D. & PEINKE, J. 2018 On universal features of the turbulent cascade in terms of non-equilibrium thermodynamics. *J. Fluid Mech.* **848**, 117–153.
RENNER, C., PEINKE, J. & FRIEDRICH, R. 2006 The Markov–Einstein coherence length—a new meaning for the Taylor length in turbulence. *Phys. Lett. A* **359** (5), 335–338.
RENNER, C., PEINKE, J., FRIEDRICH, R., CHANAL, O. & CHABAUD, B. 2002 Universality of small scale turbulence. *Phys. Rev. Lett.* **89** (12), 124502.
SAXTON-FOX, T., LOZANO-DURÁN, A. & MCKEON, B. 2022 Amplitude and wall-normal distance variation of small scales in turbulent boundary layers. *Phys. Rev. Fluids* **7** (1), 014606.
SCHMITT, F.G. 2023 Scaling analysis of time-reversal asymmetries in fully developed turbulence. *Fractal Fractional* **7** (8), 630.
SCHNAKENBERG, J. 1976 Network theory of microscopic and macroscopic behavior of master equation systems. *Rev. Mod. Phys.* **48** (4), 571.
SEIFERT, U. 2012 Stochastic thermodynamics, fluctuation theorems and molecular machines. *Rep. Prog. Phys.* **75** (12), 126001.
SMITS, A.J., MONTY, J., HULTMARK, M., BAILEY, S.C.C., HUTCHINS, N. & MARUSIC, I. 2011 Spatial resolution correction for wall-bounded turbulence measurements. *J. Fluid Mech.* **676**, 41–53.
SQUIRE, D.T., BAARS, W.J., HUTCHINS, N. & MARUSIC, I. 2016 Inner–outer interactions in rough-wall turbulence. *J. Turbul.* **17** (12), 1159–1178.
SQUIRE, D.T., HUTCHINS, N., MORRILL-WINTER, C., SCHULTZ, M.P., KLEWICKI, J.C. & MARUSIC, I. 2017 Applicability of Taylor's hypothesis in rough-and smooth-wall boundary layers. *J. Fluid Mech.* **812**, 398–417.
TALLURU, K.M., BAIDYA, R., HUTCHINS, N. & MARUSIC, I. 2014 Amplitude modulation of all three velocity components in turbulent boundary layers. *J. Fluid Mech.* **746**, R1.
TANOGAMI, T. & ARAKI, R. 2024 Information-thermodynamic bound on information flow in turbulent cascade. *Phys. Rev. Res.* **6** (1), 013090.
WALLACE, J.M. 2014 Space-time correlations in turbulent flow: a review. *Theor. Appl. Mech. Lett.* **4** (2), 022003.
WALLACE, J.M. 2016 Quadrant analysis in turbulence research: history and evolution. *Annu. Rev. Fluid Mech.* **48** (1), 131–158.
WANG, H., YANG, Z., WU, T. & WANG, S. 2021 Coherent structures associated with interscale energy transfer in turbulent channel flows. *Phys. Rev. Fluids* **6** (10), 104601.
XU, H. *et al.* 2014 Flight–crash events in turbulence. *Proc. Natl Acad. Sci. USA* **111** (21), 7558–7563.
YANG, X.I.A. & HOWLAND, M.F. 2018 Implication of Taylor's hypothesis on measuring flow modulation. *J. Fluid Mech.* **836**, 222–237.
YAO, H., YEUNG, P.K., ZAKI, T.A. & MENEVEAU, C. 2024 Forward and inverse energy cascade in fluid turbulence adhere to Kolmogorov's refined similarity hypothesis. *Phys. Rev. Lett.* **132** (16), 164001.
YAO, H., ZAKI, T.A. & MENEVEAU, C. 2023 Entropy and fluctuation relations in isotropic turbulence. *J. Fluid Mech.* **973**, R6.
ZORZETTO, E., BRAGG, A.D. & KATUL, G. 2018 Extremes, intermittency, and time directionality of atmospheric turbulence at the crossover from production to inertial scales. *Phys. Rev. Fluids* **3** (9), 094604.